

Changing the flow profile and resulting drying pattern of dispersion droplets via contact angle modification

Carmen Morcillo Perez,¹ Marcel Rey,¹ Benjamin D. Goddard,² and Job H. J. Thijssen^{1,*}

¹*SUPA School of Physics and Astronomy, The University of Edinburgh, Edinburgh, EH9 3FD, Scotland, United Kingdom*

²*School of Mathematics, The University of Edinburgh, Edinburgh, EH9 3FD, Scotland, United Kingdom*

Spilling tea or coffee leads to a tell-tale circular stain after the drying of the droplet. This phenomenon was termed after the latter example as the “coffee ring effect”. The evaporation of suspension droplets is a complex physical process, and prediction and control over particle deposit patterns obtained from sessile droplet evaporation are essential for many industrial processes such as ink-jet printing or crop-care applications. In this article, we present a systematic investigation of the effect of surface wettability on the evaporation dynamics of a particle-laden droplet, including the effect on the contact line stick-slip, the hydrodynamic flow of the suspended particles and the resulting particle deposit after evaporation. We tune the wettability of glass slides using silanisation and quantify the internal flow during the evaporation by tracking fluorescent tracer particles. We find that the internal flow shifts from a predominantly outward flow towards the contact line for low contact angles to an inward flow for large contact angles. Additionally, the corresponding deposit gradually changes from the typical coffee-ring to a central stain upon increasing the hydrophobicity of the substrate. Last, we corroborate these experimental findings with dynamic density functional theory, modelling the droplet evaporation process and stick-slip behaviour of the contact line. Our investigation suggests that the wettability of the substrate can substantially alter hydrodynamic flow within drying droplets and therefore the resulting particle deposit.

INTRODUCTION

When a drop containing disperse solids dries it leaves a solid deposit, often taking the characteristic form of a ring-like pattern, known as the coffee-ring effect (CRE) [1–3]. Robert Deegan *et al.* were the first to attribute this phenomenon to the pinning of the contact line of the droplet to the substrate [1]. They showed that liquid evaporates faster from the edges of the drop compared to its apex, inducing an outward capillary flow that carries the dispersed material to the edge of the droplet and therefore leads to a ring-like deposit [1, 4, 5].

Suspension droplet evaporation is relevant for a variety of applications such as the fabrication of transparent conductive electrodes [6], nanochromatography [7], ink-jet printing [8, 9], forensic investigations [10], crop-care applications [11–13] or diagnostics [14, 15]. However, most applications typically require a specific dried pattern, such as a uniform deposit, hence a wide range of strategies have been explored to overcome the CRE. For example, the addition of soluble surfactants [16–18] or salts [19–21], changing the particle size [22], or using various liquids [23, 24] can manipulate the hydrodynamic flow within the droplet and at least partially counteract the capillary flow and therefore improve the uniformity of the deposit. The capillary flow can also be reduced by an increase in viscosity due to the addition of soluble polymers [25] or by a gelation of the liquid [9, 26]. More complex deposition patterns were found by manipulating the temperature [27–29], electrowetting [30] or confinement [31]. Importantly, the drying behavior of suspen-

sion droplets is also affected by the substrate properties, such as its roughness [32–36] and wettability [37–40]. As a particular example, the wettability of different plant species varies from hydrophilic up to superhydrophobic [41–43]. For crop-care applications, it is therefore relevant to understand how the drying behaviour is affected by the different wettability of the specific plant leaves [11, 12].

If substrates are more hydrophobic, suspension droplets typically dry more towards the point-like shape formed in the centre of the droplet instead of a coffee ring [37–40]. Further, a change in the contact angle hysteresis was observed with a constant contact angle mode instead of a constant contact line mode for hydrophobic substrates [38, 44], which was attributed to the reduced pinning of the contact line.

Gaining further insight into the CRE from modelling of particle-laden droplets is challenging due to the interplay between thermodynamic effects, such as phase transitions and hydrodynamic effects, including fluid flow within the droplet [45]. However, a key advantage is the ability to disentangle various physical properties such as surface wettability and slip. Theoretically, a range of CAs (10, 90, 170, 180°) were explored to study the Constant Contact Angle (CCA) and Constant Contact Line (CCL) extreme modes of evaporation, however no particles were present in their calculations [46]. For CA between 0 to 90°, the Stokes flow has also been determined numerically [47]. For large CAs they predict a positive Marangoni number that leads to an inward radial flow along the droplet surface. This flow is predicted to be outward at small CAs. The effect of the initial CA on

the evolution of the flow pattern inside an evaporating sessile drop has also been numerically investigated [48]. In this case, both Marangoni flow and natural convection were found to be key for large CAs.

Here we present a systematic study of the drying behaviour of colloidal suspensions as a function of substrate wettability. We use fluorescence microscopy combined with the tracking of tracer particles to quantitatively characterise the hydrodynamic flow within the droplets during the evaporation process. Interestingly, while we observe a primarily outwards flow along the substrate for low contact angles, as expected from previous literature [1, 49, 50], the observed flow for higher contact angles becomes predominantly inwards. Additionally, upon increasing the substrate hydrophobicity, the dried deposit gradually changes from the typical coffee-ring to a dot-like deposit. This reveals that modifying the substrate wettability could be a new way of obtaining a desired deposit without the need to alter the liquid formulation or ambient conditions. Finally, we complement our experimental results with dynamic density functional theory simulations to verify the droplet evaporation behaviour and to elucidate the role of the stick-slip behaviour of the contact line.

MATERIALS AND METHODS

Dispersion preparation

All droplets used were $1 \mu\text{l}$ in volume and contain 0.1 %w of red fluorescent carboxylate-modified polystyrene latex beads in aqueous suspension (mean particle diameter $1.90 \mu\text{m}$, Sigma-Aldrich) and 0.0005 %w of yellow-green fluorescent carboxylate-modified polystyrene latex beads in aqueous suspension (mean particle diameter $1.90 \mu\text{m}$, Sigma-Aldrich) in distilled and de-ionized water ($18 \text{ M}\Omega\text{cm}$, Milli-Q RG Opak). The dispersion was centrifuged and the surface tension of the supernatant water was measured to be 73 mN m^{-1} (with a Krüss DSA100 drop tensiometer model 65 FM40Mk2) which aligns well with literature values for a clean air-water interface at 21°C [51], suggesting that there was no interfacially active contamination in the supernatant. The beads were imaged with a Confocal Microscope (Zeiss LSM 700) and Scanning Electron Microscope (SEM, JEOL, 6010 LV, 20kV, 15 nm gold-coated samples) to assess overall round appearance, and to confirm that particle size aligns with supplier information.

Substrate preparation

Four types of glass substrates were prepared in order to study different water contact angles. All glass substrates

(Cat. No. 7101, Scientific Glass Laboratories ltd., Tunstall) were cleaned prior to use or functionalisation.

For the cleaning stage the slides were first submerged in a 5 % Decon 90 (R) cleaning solution (used as sold, Decon Laboratories Limited) in distilled and deionised water ($18 \text{ M}\Omega\text{cm}$, Milli-Q RG Opak) and sonicated for 10 minutes in an ultrasonic cleaner (USC200T, VWR ultrasonic cleaner, frequency 45 kHz, max. output power 120 W, Ultraschall Sonic Ultrasons). These were then rinsed with distilled and deionised water to eliminate any potential Decon residue. Finally, the glass slides were plasma-treated (Zepto, model 2, Diener Electronic) for 10 seconds at 35 W.

For the silanisation step, the cleaned substrates were submerged in a solution of 40 mL ethanol ($\geq 99.8 \text{ \%}$, Sigma-Aldrich) and 4 mL aqueous ammonia solution (35 %, Fisher Chemicals). One slide was functionalised with $50 \mu\text{l}$ of 1H,1H,2H,2H-Perfluoro-octyltrithoxysilane (FOTS) (98 %, Sigma-Aldrich) giving initial CAs of $105.3 \pm 1.9^\circ$. Two slides were functionalised with 1 mL and 3 mL of 1,1,1,3,3,3-Hexamethyldisilazane (HMDS) (99 %, Fluka Analytical), giving initial CAs of $54.6 \pm 1.3^\circ$ and $95.2 \pm 2.6^\circ$, respectively. The glass slides were submerged in the mixture for 72 hours with continuous stirring. The samples were then cleaned with ethanol and sonicated in a bath ultrasonic cleaner in order to remove potential silane multilayers. The final slide was not functionalised and kept pristine after the cleaning stage, giving initial CAs of $37.7 \pm 1.0^\circ$.

Side-view imaging

The dispersion was loaded into a glass syringe (Hamilton, 450 μl) with a stainless steel needle (with luer-lock, 0.499 mm diameter) connected to a software-controlled dosing system. A $1 \mu\text{l}$ drop was generated and gently placed on the substrate. To capture image sequences of the drop we used a Drop Shape Analyser (DSA100, Krüss, model 65 FM40Mk2) with a charge-coupled device camera (Stingray) controlled by a PC. The focal plane was positioned across the middle of the droplet when generated. The image sequences were later analysed using an in-house Matlab code that calculates the CA, height, base diameter and volume for every frame. The code used a fitting method based on a circle fit by Taubin [52]. All the contact angles were measured at least three times, by depositing a new droplet in a different spot on the substrate. The mean of the CA was used for the analysis and plotting.

Fluorescence Microscopy

A $1 \mu\text{l}$ drop was carefully deposited onto the substrate with a micropipette (0.5 - $10 \mu\text{l}$, TopPette Pipet-

tor). A semi-automated upright epi-fluorescence microscope (Nikon Eclipse E800) with a camera (QImaging Retiga 2000R Fast 1394 Cooled) and a Nikon CFI Plan Fluor objective (10 \times magnification, NA 0.30, WD 16 mm) was used to take images of the drop every 2 seconds throughout the evaporation process, with the focal plane just above the solid-liquid interface. The illumination filter sets used were EGFP excitation filter (Chroma ET470/40x) and EGFP emission filter (Chroma ET525/50m) for the particle tracking; and mCherry excitation filter (Chroma ET572/35x) and mCherry emission filter (Chroma ET632/60m) for the imaging of the dried deposit. The system was enclosed in an incubator chamber at all times for monitored temperature (19 \pm 2°) and humidity (46 \pm 2 %).

DDFT Model

DDFT describes the time evolution of ensemble-averaged densities for the liquid (ρ^ℓ) and particles (ρ^n) in a droplet. These densities evolve according to a pair of coupled partial differential equations (PDEs):

$$\partial_t \rho^\ell(\mathbf{x}, t) = \nabla \cdot \left[M^\ell(\mathbf{x}, \rho^\ell, \rho^n) \rho^\ell \nabla \frac{\delta \mathcal{F}[\rho^\ell, \rho^n]}{\delta \rho^\ell} \right] \quad (1)$$

$$\partial_t \rho^n(\mathbf{x}, t) = \nabla \cdot \left[M^n(\mathbf{x}, \rho^\ell, \rho^n) \rho^n \nabla \frac{\delta \mathcal{F}[\rho^\ell, \rho^n]}{\delta \rho^n} \right]. \quad (2)$$

Here \mathbf{x} is the spatial coordinate; t is time; M^ℓ and M^n are the mobility coefficients for the liquid and nanoparticles, respectively; and \mathcal{F} is the Helmholtz free energy. Note that typically $\rho^n \ll \rho^\ell$ in the initial condition, representing a dilute mixture. The boundary conditions are no-flux at the substrate, evaporative at the top of the domain, and periodic on the boundaries perpendicular to the substrate. Our initial conditions are smoothed spherical caps. See Supplementary Information for further details of the model.

Our model is taken from previous work on the evaporation of particle-laden droplets [53]. In [53], the dynamics are discretised onto a lattice, with the value of ρ^ℓ at a lattice site \mathbf{i} denoted ρ_i^ℓ , and analogously for other quantities, giving

$$\begin{aligned} \partial_t \rho_i^\ell &= \nabla \cdot \left[M_i^\ell \rho_i^\ell \nabla \frac{\delta \mathcal{F}}{\delta \rho_i^\ell} \right], \\ \partial_t \rho_i^n &= \nabla \cdot \left[M_i^n \rho_i^n \nabla \frac{\delta \mathcal{F}}{\delta \rho_i^n} \right]. \end{aligned} \quad (3)$$

The Helmholtz free energy is approximated using a mean field approach. See references within [53] for a justification of this, and the Supplementary Information for the precise form of \mathcal{F} . We take the same approach as in [53] and average the equations into two dimensions with corresponding coefficients given in the Supplementary Information.

It remains to describe the mobilities in equation (3), as well as the boundary conditions for the lattice dynamics. For the mobilities, we take

$$M_i^c = \begin{cases} m_i^c \begin{pmatrix} s & 0 & 0 \\ 0 & \nu & 0 \\ 0 & 0 & s \end{pmatrix} & j = 1 \\ m_i^c \begin{pmatrix} 1 & 0 & 0 \\ 0 & 1 & 0 \\ 0 & 0 & 1 \end{pmatrix} & \text{otherwise} \end{cases} \quad (4)$$

Here s and ν determine the slip at the substrate, with s controlling motion parallel to the substrate ($s = 0$ for a no-slip substrate), while ν prevents ‘hopping’ of particles; typically $\nu \ll 1$. If $\nu \approx 1$ then the choice of $s = 0$ no longer enforces a no-slip condition at the substrate as the liquid or particle migrates to the $j = 2$ layer, moves parallel to the substrate, and then returns to the $j = 1$ layer next to the substrate. We assume that the liquid mobility is constant $m_i^\ell = m_\ell$, while that of the particles depends on the density (i.e., the number of particles in a cell in the microscopic model) of the liquid: $m_i^n = \frac{m_n}{2} [\tanh(8\rho_i^\ell - 4) + 1]$. This enforces that the particles do not move on a dry surface, but move freely when they are surrounded by liquid. The particular choice of m_i^n is arbitrary, but once again we have followed [53], and the function smoothly interpolates between no particle motion when dry to free motion when ‘completely wet’.

We note that, for a fixed initial condition, the size of the domain affects the speed of evaporation, with droplets in smaller boxes evaporating more rapidly. We choose the domain to be sufficiently large (70 \times 140) so that the only change in the dynamics observed by increasing or decreasing the size of the box is in the evaporation timescale – the dynamics are unchanged after a time rescaling. We use the numerical method described in the Appendix of [53] with $k_B T = 1$, $\epsilon_{\ell\ell} = 1.5$, and a timestep of 10^{-2} for no-slip dynamics ($s = 0$) and 5×10^{-3} when $s = 1$. For the two smallest contact angles, we deviate very slightly from the experimental means, due to the initial transient dynamics observed in the experiments. In particular, for contact angles [105°, 95°, 55°, and 38°], we choose $\epsilon_{w\ell} = [0.32, 0.39, 0.74, 0.84]\epsilon_{\ell\ell}$, which corresponds to initial simulation contact angles of [105°, 95°, 52°, 35°]. Note that this choice has very little effect on the overall dynamics of the systems.

RESULTS AND DISCUSSION

We first investigated the effect of the wettability of the substrates on the droplet CA and the resulting drying pattern (figure 1). Although a small variation is observed between the repeats, the overall appearance of the deposits look qualitatively similar. The deposits for all the repeats can be seen in the Supplementary Information.

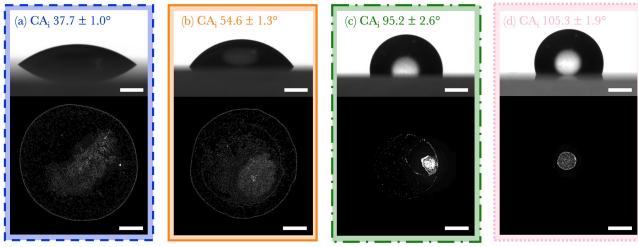


FIG. 1. Droplet shape (top) and dried deposit (bottom) as a function of substrate wettability. Top: Side-view images of $1 \mu\text{l}$ water droplets containing fluorescent particles on four different silanised glass substrates. Bottom: Stitched fluorescence microscopy images of the dried particle dispersion. CA_i refers to the initial CA calculated using image analysis from a side-view image of the droplet. Scale bars: 0.5 mm.

A CRE is clearly observed for the substrate with smallest CA, $CA_i = 38^\circ$. The deposit for the substrate with $CA_i = 55^\circ$ also shows CRE; however, it is less clear as depinning is likely to have occurred leaving a second less clear smaller ring circumscribed. The dried pattern in the substrate with $CA_i = 95^\circ$ shows signs of multiple depinning steps and a continuous ring is not visible, but instead shows numerous discontinuous ring deposits and a bright spot of concentrated particles. The substrate with the biggest CA, $CA_i = 105^\circ$, stands out because of the small bright spot that is the main visible feature of the deposit. Upon closer inspection of this sample it is possible to see radial particle deposits, likely caused by a continuous inwards slip motion of the droplet, that leads to a very thin discontinuous ring-like deposit.

Similar behaviour has been reported analytically in the literature [54, 55]. They calculated that the final dried pattern depends on the flow within the drop; this flow is dependent on the evaporative flux, shape of the free surface, and behaviour of the contact line. Subject to these factors, the flow can be inwards, outwards or a mixture. We therefore decided that a more exhaustive analysis is needed so we recorded the evaporation process from a side-view and a top-view and compared it to the results from a DDFT model.

Dynamic side-view analysis

Image sequences of droplets drying were recorded from the side for each of the different substrates. An in-house MATLAB image analysis code was used to calculate the CA, base diameter, height and volume for each of the images. The images at $time = 0$ can be seen in figure 1 accompanied by the initial CA extracted. After taking three repeats per substrate we determined that although a small variation is observed, the overall shape of the evaporation curves are reproducible for the different substrates (figure 2).

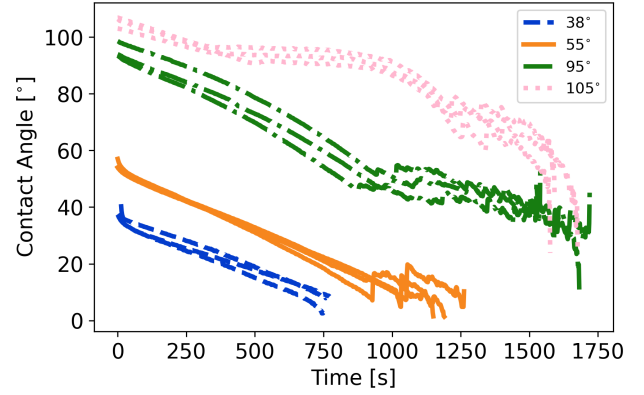


FIG. 2. Graph showing the evolution of contact angle with evaporation time for four different silanised glass substrates. Data calculated using an in-house MATLAB image analysis code from side-view images. The CA in the legend refers to the average initial CA at $t = 0$.

At first glance, substrates with $CA_i = 38^\circ$, 55° and 95° appear to have fairly similar wetting profiles (figure 2). For all three, the first stage of the evaporation seems to be of constant contact line (CL), as seen by the continuously decreasing CA. This stage is followed by a mixed dynamic of both moving CL and changing CA. Similarly, the substrate with $CA_i = 105^\circ$ has an initial stage of constant CL, however this is shorter and followed by a constant CA stage, which is not seen for any other substrate. The final part of evaporation appears as a mixed mode of both moving CL and changing CA for all substrates. These findings are in agreement with previous studies, where droplets also evaporate via a combination of “stick” and “slide” phases [38, 44, 46]. Note that, occasionally, we observed asymmetric CL motion, where the droplet depinning only occurs on one side of the droplet.

From this experiment we conclude that different initial CAs do not necessarily lead to a qualitatively different external drying behaviour (substrates with $CA_i = 38^\circ$, 55° and 95°). The word external is referring to the mere observation of the outer profile of the drop. Yet, because qualitatively different dried deposits have previously been observed (figure 1), analysis of the internal flows of the droplet will likely be key to understanding these differences (see section 3.2). Additionally, different external drying behaviours are observed even for similar initial CA (see curves for substrates with $CA_i = 95^\circ$ and $CA_i = 105^\circ$). Hence, the surface chemistry of the substrate may also play a key role.

DDFT simulations have been performed to model the droplet evaporation process and the corresponding results are shown in figure 3. Unless otherwise stated we use $\nu = 1 \cdot 10^{-5}$, giving good agreement with the experimental results where a constant contact line mode is dominant throughout the evaporation process (sub-

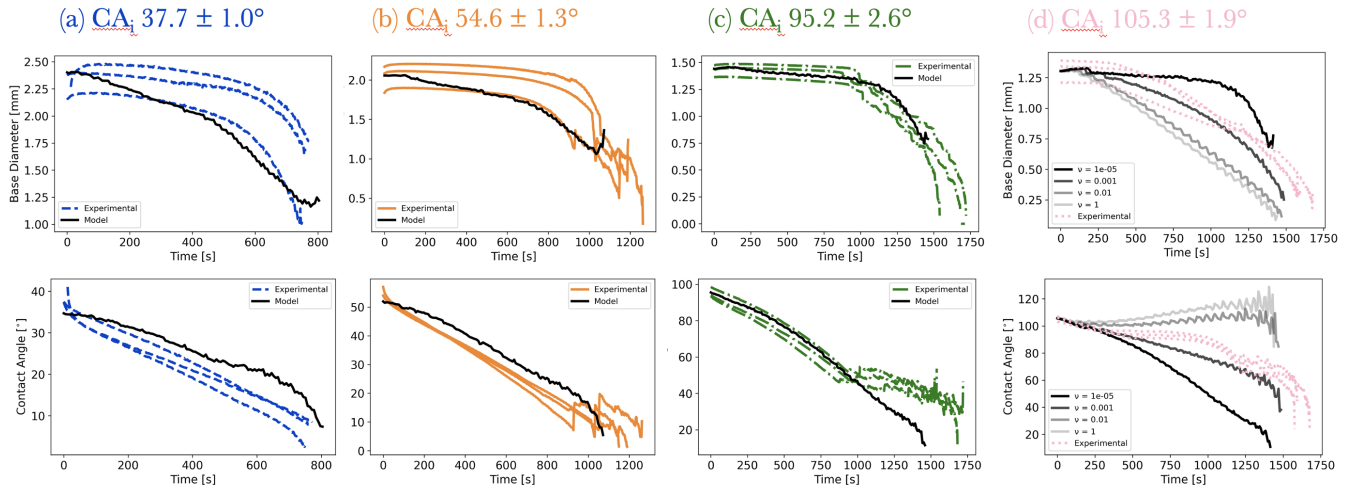


FIG. 3. Graphs showing the evolution of base diameter (top) and contact angle (bottom) with evaporation time for four different silanised glass substrates. Data calculated using an in-house MATLAB image analysis code from side-view images. The CA in the legend refers to the average initial CA at $t = 0$. The black lines represent the DDFT simulations for $\nu = 1 \cdot 10^{-5}$ unless otherwise specified.

strates with $CA_i = 38, 55$ and 95°). However, for the substrate with $CA_i = 105^\circ$, a range of ν parameters are presented, showing that this can be applied to tailor the stick-slip behaviour of the substrate. In other words, the simulations can also reproduce the observed behaviour for $CA_i = 105^\circ$ by choosing an appropriate value for the parameter ν . As a different silanising agent was used to prepare this substrate, it is perhaps not surprising that a different value of ν fits the experimental data better. We note that ν likely depends on local surface properties, such as heterogeneities, and there is no mechanism in the model for switching ν over time, which would allow a more accurate reproduction of the experimental results for $CA_i = 105^\circ$; this is an interesting topic for future work. Note that these simulations were performed with no particles, i.e., $\rho^n = 0$; simulations with low particle concentrations show essentially identical results except in the final stages of evaporation. Results including particles can be found in the Supplementary Information.

The model aims to enforce the constant CL condition by restricting the mobility of the water and particles in the cells closest to the substrate. This prevents movement parallel to the substrate and strongly limits movement perpendicular to the surface, preventing ‘hopping’ [53]. This seems to work well in the cases of large contact angles; see videos in corresponding data files. In contrast, in the case of small contact angles, the water forms a film in the layer above the substrate. This film layer is indeed fixed, but then the droplet evolves above this layer, leading to a more constant CA-like behaviour. This is likely a consequence of the increased water-substrate attraction versus the water-water interactions, compared to the larger contact angle cases; this is needed to ensure the correct equilibrium contact angle.

Dynamic top-view particle tracking

The droplet evaporation was recorded from the top using fluorescence microscopy to track tracer particles. An EGFP filter is used, to track only the green-dyed beads (concentration = 0.0005 %), although the total concentration of particles is 0.1 %, with the remaining particles being red-dyed beads (see methods for further information). The image sequences are analysed in Python with a particle tracking code based on the TrackPy module [56]. The particles are identified in each of the images, linked from frame to frame and filtered using an implementation of the Crocker-Grier linking algorithm [57]. Basic initial and filtering parameters have to be set and can be found in the Supplementary Information.

The location of each particle throughout the evaporation process is shown in figure 4 (top row), where the colour refers to the time after the drop has been deposited. Most particles seem to have a radial trajectory, towards the centre or edge of the drop. In order to quantify this, the position of the centre of the drop is subtracted from the position of each particle and the absolute values are plotted against evaporation time, as seen in figure 4 (bottom row), where the slope of the curves are related to the velocity of each particle. Note that the position of the droplet centre is chosen by eye and is kept the same throughout the analysis. If the CL depinning is asymmetric, the centre of the drop may change slightly over time. However, looking at figure 4 (top row), the chosen centre seems to be consistent with the particles’ trajectories.

There is a notable change in the direction of the particles from the substrate with the smallest CA to the one with the highest. To quantify this change, the ratio of

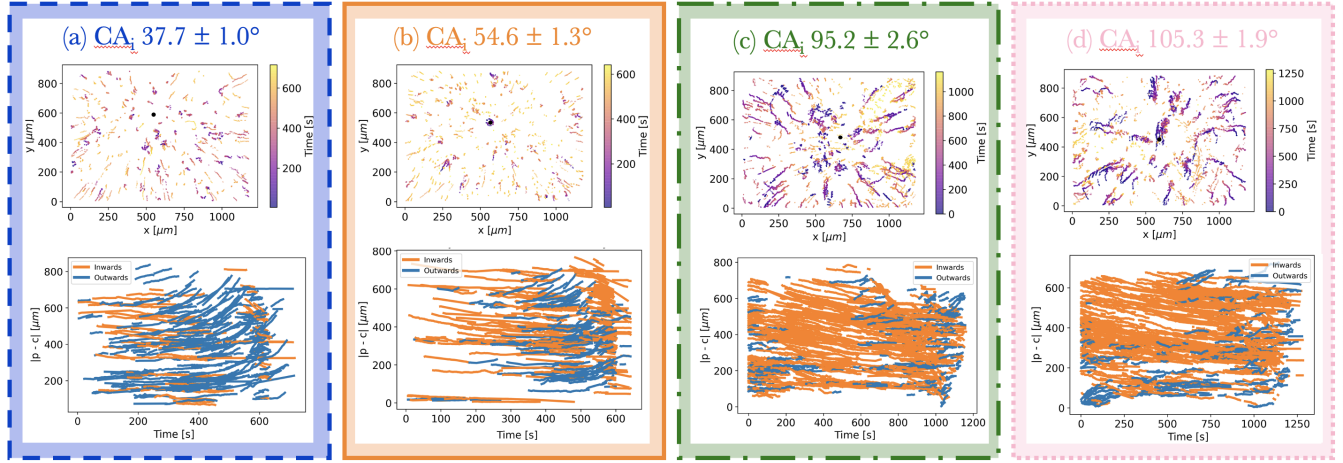


FIG. 4. Top: Position of the tracer particles throughout the evaporation process. The colour gradient indicates the time after the drop was deposited. A black dot indicates the centre of the drop. The focal plane was located just above the substrate. Bottom: Absolute distance between an individual particle (p) and the droplet centre (c) with time. If the slope is positive the particle is deemed as going 'outwards' or towards the edges of the drop; if the slope is negative, it is deemed as going 'inwards' or towards the centre of the drop.

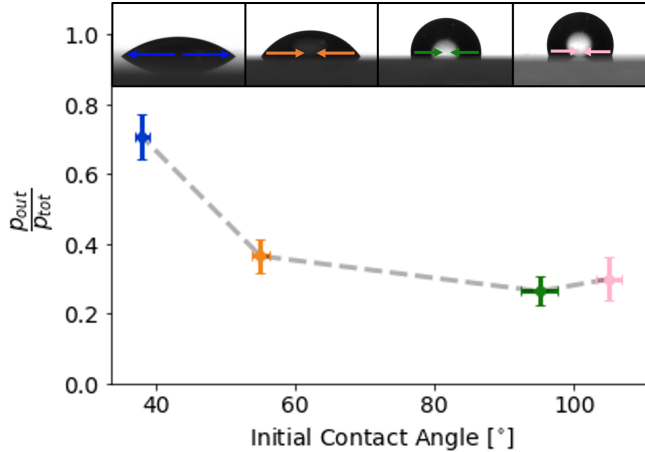


FIG. 5. Top: Schematic of the predominant flow of particles for each different substrate. Bottom: ratio of particles going outwards versus initial contact angle. Dashed line is a guide to the eye.

particles going towards the edges of the drop against the total number of particle trajectories has been plotted in figure 5 for all the experiments performed, showing an increase in the ratio of particles going towards the centre with increasing CA.

For the pristine glass substrate, $CA_i = 38^\circ$, the predominant outward flow agrees with observations made in the literature and suggests a coffee-ring formation due to capillary outward flow [1, 49, 50]. For the hydrophobic substrates, the predominant inward direction of the flow observed close to the solid-liquid contact line agrees with the results from the numerical studies performed on droplets of a NaCl solution [20, 58]; note that we have

not added any NaCl to our dispersions here. They evaluated the internal fluid flow for a drop of spherical shape and 160° contact angle. Further studies have tried to analytically calculate the form and direction of the internal evaporative flows for pinned/moving contact line and hydrophobic/hydrophilic CA. It was reported that a predominant outward flow is found when the CL is pinned, and for a moving CL if the substrate is hydrophobic. If the substrate is hydrophilic, they found a predominant inward flow when the CL is not pinned [55]. These results only partially agree with our experimental observations. In our experiments, all substrates but the one with $CA_i = 105^\circ$ exhibit a predominantly constant CL. However, only the one with the smallest CA, $CA_i = 38^\circ$, has a predominant outward flow. We rule out that the slip of the CL is causing this inward flow as it is also observed for the substrate with $CA_i = 95^\circ$ which has a pinned CL for most of the evaporation process (figure 2 green dotted-dashed line in the region for time: 0-800 s) whereas the majority of particles go inwards for that time frame (figure 4 (c) bottom).

Further particle velocimetry analysis has been performed to validate these observations. We define a radial velocity as positive when going towards the CL and negative when going towards the centre of the drop. Thus, we observe that the average velocity of moving particles decreases with increasing CA (figure 6). This agrees with the particle tracking results where we obtain that the ratio of particles going towards the CL decreases with increasing CA (figure 5). Additionally, a closer look to figure 4 bottom, elucidates that particles going outwards move faster than particles going towards the centre of the drop.

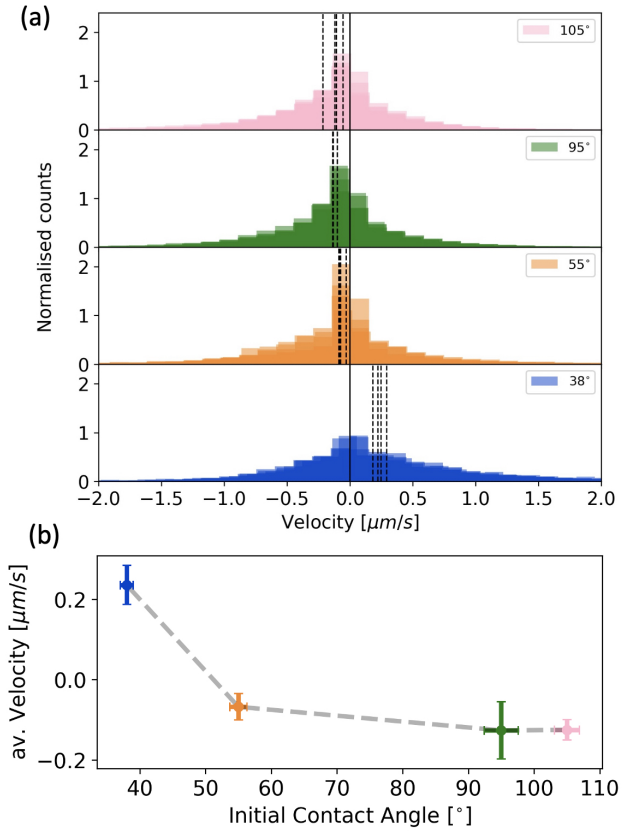


FIG. 6. (a) Histograms of velocity for the different substrates. Counts are normalised so that the area under the histogram integrates to 1. Vertical dashed lines refer to the average velocity for each repeat (4 repeats per substrate shown overlaid). Vertical solid line at velocity = $0 \mu\text{m/s}$ is a guide to the eye. (b) Average velocity of moving particles plotted against the initial contact angle of the substrate. Line is a guide to the eye.

For this analysis, particles with an absolute velocity of less than $0.037 \mu\text{m/s}$ are considered stuck and as such they are not included in the velocity calculations. A minimum cut-off velocity is required to eliminate particles that are stuck on the substrate, particularly at later stages of evaporation. Assuming that the particle tracking resolution is $1/10$ of a pixel at best [57], particles with an apparent velocity of $0.037 \mu\text{m/s}$ or smaller should be considered stuck. We also decided to do an experimental check by identifying, linking, tracking and calculating the velocity of particles that do not move (outside of the droplet edge). For these we get an average velocity of $0.034 \mu\text{m/s}$ which is in good agreement with the minimum cut-off based on the resolution argument.

In the remainder of this section we speculate on the explanation for the observed drying behaviour and link it to the internal flow within the droplets and the resulting change in contact line stick-slip behaviour. For a low initial contact angle ($CA_i = 38^\circ$), we observe primarily

a capillary outward flow leading to the formation of an initial coffee ring. The initial coffee ring induces a strong pinning of the contact line and therefore we observe a constant contact line mode (figure 2). On the other hand, on the substrate with a high contact angle ($CA_i = 105^\circ$) we measure the opposite flow from the contact line towards the centre. We interpret that this change in the flow profile prevents the formation of a coffee ring at the drop edge and therefore leads to a reduced pinning of contact line (substrate with $CA_i = 105^\circ$, figure 2). This, in turn, may explain the observed constant contact angle mode and therefore the shift from a typical coffee ring deposit to a central spot-like deposit. A similar observation was made in previous research where a dot-like deposit was found for an inward flow and a typical CRE for outward flow [59]. Interestingly, for the substrate with a contact angle of $CA_i = 95^\circ$ we observe a mixture of both behaviours. While the flow within the droplet is still primarily inwards, we observe some pinning of the contact line (figures 1 and 2, green dotted-dashed line), but the droplet still dries into a central spot. For a contact angle of $CA_i = 55^\circ$ the pinning is increased and the deposit is a coffee ring. This indicates that there may be a gradual transition between the two extreme drying modes. We should, however, note that $CA_i = 38$, 55 and 95° and $CA_i = 105^\circ$ substrates were modified using different silanizing agents, which should be kept in mind when comparing, for example, $CA_i = 95^\circ$ and $CA_i = 105^\circ$ results.

CONCLUSIONS

This article studies the role played by the initial CA in altering the evaporative flows in a sessile droplet. The fabricated substrates with systematically tuned wettability exhibit distinctive evaporation modes, identified throughout the droplet lifetime, with characteristic dried deposits found for each initial CA.

Both in the experimental and DDFT modelling analysis we find very similar behaviours for the CA and base diameter versus time for intermediate initial CAs. The percentage of particles moving towards the centre of the drop increases with increased initial CA, and we have observed a concurrent shift from the expected coffee-ring-like deposit to a smaller disk-like deposit featuring a more uniform distribution of the particles. Therefore, we interpret that for hydrophobic substrates the change in the flow profile prevents the formation of a coffee ring at the drop edge and that this flow is not caused by the slip motion of the CL. However the lack of particles at the CL may, in turn, favour the slip motion.

An explanation for the results obtained is that for CAs larger than 90° geometrical constraints could lower the rate of evaporation at the triple phase contact line compared to the apex of the droplet. Therefore, particles

are no longer pushed towards the edges of the drop and instead pushed towards the centre, leaving a dot-like deposit.

To summarise, our study suggests that the initial CA of the substrate can substantially alter the flow within drying suspension droplets and therefore alter the morphology of the resulting deposit.

CONFLICTS OF INTEREST

There are no conflicts to declare.

ACKNOWLEDGEMENTS

C.M.P. and J.H.J.T. thank Laura Edwards, Kathryn Knight, Marie-Capucine Pope and Martin Shaw at Croda (UK) for useful discussions. C.M.P. acknowledges studentship funding from the EPSRC Centre for Doctoral Training in Soft Matter and Functional Interfaces (SOFI-CDT, EP/L015536/1). M.R. acknowledges the Swiss National Science Foundation Project-ID P2SKP2-194953. B.D.G. thanks Andrew Archer for helpful discussions. The authors also acknowledge SOFI CDT and EPSRC for financial support for the electron microscope used in this project.

* j.h.j.thijssen@ed.ac.uk

- [1] R. D. Deegan, O. Bakajin, T. F. Dupont, G. Huber, S. R. Nagel, and T. A. Witten, *Nature* **389**, 827 (1997).
- [2] H. Hu and R. G. Larson, *The Journal of Physical Chemistry B* **106**, 1334 (2002).
- [3] D. Mampallil and H. B. Eral, *Advances in colloid and interface science* **252**, 38 (2018).
- [4] R. D. Deegan, *Physical Review E - Statistical Physics, Plasmas, Fluids, and Related Interdisciplinary Topics* **61**, 475 (2000).
- [5] R. D. Deegan, O. Bakajin, T. F. Dupont, G. Huber, S. R. Nagel, and T. A. Witten, *Physical Review E - Statistical Physics, Plasmas, Fluids, and Related Interdisciplinary Topics* **62**, 756 (2000).
- [6] M. Layani, M. Gruchko, O. Milo, I. Balberg, D. Azulay, and S. Magdassi, *ACS Nano* **3**, 3537 (2009).
- [7] T.-S. Wong, T.-H. Chen, X. Shen, and C.-M. Ho, *Analytical Chemistry* **83**, 1871 (2011).
- [8] Y.-H. Son, M. K. Kang, and C. S. Lee, *Materials Chemistry and Physics* **223**, 779 (2019).
- [9] E. L. Talbot, L. Yang, A. Berson, and C. D. Bain, *ACS Applied Materials & Interfaces* **6**, 9572 (2014).
- [10] F. Smith and D. Brutin, *Current Opinion in Colloid and Interface Science* **36**, 78 (2018).
- [11] M. Hunsche and G. Noga, *Pest Management Science* **68**, 231 (2012).
- [12] Y. Yu, H. Zhu, J. M. Frantz, M. E. Reding, K. C. Chan, and H. E. Ozkan, *Biosystems Engineering* **104**, 324 (2009).
- [13] Y. Li, C. Diddens, T. Segers, H. Wijshoff, M. Versluis, and D. Lohse, *Proceedings of the National Academy of Sciences of the United States of America* **117**, 16756 (2020).
- [14] C. P. Gulka, J. D. Swartz, J. R. Trantum, K. M. Davis, C. M. Peak, A. J. Denton, F. R. Haselton, and D. W. Wright, *ACS applied materials & interfaces* **6**, 6257 (2014).
- [15] S. Devineau, M. Anyfantakis, L. Marichal, L. Kiger, M. Morel, S. Rudiuk, and D. Baigl, *Journal of the American Chemical Society* **138**, 11623 (2016).
- [16] H. Yildirim Erbil, *Advances in Colloid and Interface Science* **222**, 275 (2015).
- [17] T. Still, P. J. Yunker, and A. G. Yodh, *Langmuir* **28**, 4984 (2012).
- [18] A. Marin, R. Liepelt, M. Rossi, and C. J. Kähler, *Soft Matter* **12**, 1593 (2016).
- [19] A. Marin, S. Karpitschka, D. Noguera-Marín, M. A. Cabrerizo-Vilchez, M. Rossi, C. J. Kähler, and M. A. Rodríguez Valverde, *Physical Review Fluids* **4**, 41601 (2019).
- [20] T. K. Pradhan and P. K. Panigrahi, *Colloids and Surfaces A: Physicochemical and Engineering Aspects* **500**, 154 (2016).
- [21] T. A. Nguyen, M. A. Hampton, and A. V. Nguyen, *Journal of Physical Chemistry C* **117**, 4707 (2013).
- [22] D. Parthasarathy, S. P. Thampi, P. Ravindran, and M. G. Basavaraj, *Langmuir* **37**, 4395 (2021).
- [23] J. Pyeon and H. Kim, *Soft Matter* **17**, 3578 (2021).
- [24] H. Hu and R. G. Larson, *The Journal of Physical Chemistry B* **110**, 7090 (2006).
- [25] L. Cui, J. Zhang, X. Zhang, L. Huang, Z. Wang, Y. Li, H. Gao, S. Zhu, T. Wang, and B. Yang, *ACS applied materials & interfaces* **4**, 2775 (2012).
- [26] H. Li, D. Buesen, R. Williams, J. Henig, S. Staph, K. Mukherjee, E. Freier, W. Lubitz, M. Winkler, T. Happe, and N. Plumeré, *Chemical Science* **9**, 7596 (2018).
- [27] V. D. Ta, R. M. Carter, E. Esenturk, C. Connaughton, T. J. Wasley, J. Li, R. W. Kay, J. Stringer, P. J. Smith, and J. D. Shephard, *Soft Matter* **12**, 4530 (2016).
- [28] M. Parsa, S. Harmand, K. Sefiane, M. Bigerelle, and R. Deltombe, *Langmuir* **31**, 3354 (2015).
- [29] Y. Li, C. Lv, Z. Li, D. Quéré, and Q. Zheng, *Soft Matter* **11**, 4669 (2015).
- [30] H. B. Eral, D. M. Augustine, M. H. Duits, and F. Mugele, *Soft Matter* **7**, 4954 (2011).
- [31] R. Mondal and M. G. Basavaraj, *Soft Matter* **16**, 3753 (2020).
- [32] P. Kabi, V. Razdan, D. Roy, L. Bansal, S. Sahoo, R. Mukherjee, S. Chaudhuri, and S. Basu, *Soft Matter* **17**, 1487 (2021).
- [33] S. Li, M. Dong, R. Li, L. Zhang, Y. Qiao, Y. Jiang, W. Qi, and H. Wang, *Nanoscale* **7**, 18453 (2015).
- [34] M. Dicuagco, S. Dash, J. A. Weibel, and S. V. Garimella, *Applied Physics Letters* **104**, 201604 (2014).
- [35] P. Brunet, *Soft Matter* **8**, 11294 (2012).
- [36] A. Lafuma and D. Quéré, *Europhysics Letters* **96**, 56001 (2011).
- [37] R. Iqbal, B. Majhy, A. Q. Shen, and A. K. Sen, *Soft Matter* **14**, 9901 (2018).
- [38] S. Y. Lin, K. C. Yang, and L. J. Chen, *Journal of Physical Chemistry C* **119**, 3050 (2015).

[39] Y. F. Li, Y. J. Sheng, and H. K. Tsao, *Langmuir* **29**, 7802 (2013).

[40] P. L. Kumar, S. P. Thampi, and M. G. Basavaraj, *Journal of Physics: Condensed Matter* **33**, 024003 (2021).

[41] H. Fang, Z. Zhang, S. Xiao, and Y. Liu, *Journal of Agriculture and Food Research* **1**, 100011 (2019).

[42] E. Papierowska, S. Szporak-Wasilewska, J. Szewińska, J. Szatylowicz, G. Debaene, and M. Utratna, *Trees* **32**, 1253 (2018).

[43] V. Fernández, H. A. Bahamonde, J. J. Peguero-Pina, E. Gil-Pelegrín, D. Sancho-Knapik, L. Gil, H. E. Goldbach, and T. Eichert, *Journal of Experimental Botany* **68**, 5293 (2017).

[44] K.-C. Yang, C. Wang, T.-Y. Hu, H.-P. Lin, K.-H. Cho, and L.-J. Chen, *Journal of Colloid and Interface Science* **579**, 212 (2020).

[45] X. Zhong, A. Crivoi, and F. Duan, *Advances in colloid and interface science* **217**, 13 (2015).

[46] J. M. Stauber, S. K. Wilson, B. R. Duffy, and K. Sefiane, *Langmuir* **31**, 3653 (2015).

[47] H. Hu and R. G. Larson, *Langmuir* **21**, 3972 (2005).

[48] Y. Chen, F. Hong, and P. Cheng, *International Communications in Heat and Mass Transfer* **112**, 104493 (2020).

[49] M. Parsa, S. Harmand, and K. Sefiane, *Advances in Colloid and Interface Science* **254**, 22 (2018).

[50] D. Zang, S. Tarafdar, Y. Y. Tarasevich, M. Dutta Choudhury, and T. Dutta, *Physics Reports* **804**, 1 (2019).

[51] N. B. Vargaftik, B. N. Volkov, and L. D. Voljak, *Journal of Physical Chemistry* **12**, 817 (1983).

[52] G. Taubin, *IEEE Transactions on Pattern Analysis and Machine Intelligence* **13**, 1115 (1991).

[53] C. Chalmers, R. Smith, and A. Archer, *Langmuir* **33**, 14490 (2017).

[54] H. Masoud and J. D. Felske, *Physics of Fluids* **21**, 1 (2009).

[55] H. Masoud and J. D. Felske, *Physical Review E - Statistical Physics, Plasmas, Fluids, and Related Interdisciplinary Topics* **79**, 016301 (2009).

[56] D. B. Allan, T. Caswell, N. C. Keim, and C. M. van der Wel, “soft-matter/trackpy: Trackpy v0.4.2,” (2019), <https://doi.org/10.5281/zenodo.3492186>.

[57] J. C. Crocker and D. G. Grier, *Journal of Colloid and Interface Science* **179**, 298 (1996).

[58] T. K. Pradhan and P. K. Panigrahi, *Colloids and Surfaces A: Physicochemical and Engineering Aspects* **530**, 1 (2017).

[59] R. Malinowski, G. Volpe, I. P. Parkin, and G. Volpe, *The Journal of Physical Chemistry Letters* **9**, 659 (2018).